

A study of the hydrostatic mass bias dependence and evolution within THE THREE HUNDRED clusters

Giulia Gianfagna,^{1,2}★ Elena Rasia,^{3,4} Weiguang Cui,^{5,6} Marco De Petris,² Gustavo Yepes,^{6,7}

Ana Contreras-Santos,⁶ and Alexander Knebe,^{6,7,8}

¹INAF, Istituto di Astrofisica e Planetologia Spaziali, via Fosso del Cavaliere 100, 00133 Rome, Italy

²Dipartimento di Fisica, Sapienza Università di Roma, Piazzale Aldo Moro, 5-00185 Roma, Italy

³IFPU - Institute for Fundamental Physics of the Universe, Via Beirut 2, 34014 Trieste, Italy

⁴INAF Osservatorio Astronomico di Trieste, via Tiepolo 11, I-34131, Trieste, Italy

⁵Institute for Astronomy, University of Edinburgh, Royal Observatory, Edinburgh EH9 3HJ, UK

⁶Departamento de Física Teórica, Módulo 15, Facultad de Ciencias, Universidad Autónoma de Madrid, E-28049 Madrid, Spain

⁷Centro de Investigación Avanzada en Física Fundamental (CIAFF), Facultad de Ciencias, Universidad Autónoma de Madrid, 28049 Madrid, Spain

⁸International Centre for Radio Astronomy Research, University of Western Australia, 35 Stirling Highway, Crawley, Western Australia 6009, Australia

Accepted XXX. Received YYY; in original form ZZZ

ABSTRACT

We use a set of about 300 simulated clusters from THE THREE HUNDRED Project to calculate their hydrostatic masses and evaluate the associated bias by comparing them with the true cluster mass. Over a redshift range from 0.07 to 1.3, we study the dependence of the hydrostatic bias on redshift, concentration, mass growth, dynamical state, mass, and halo shapes. We find almost no correlation between the bias and any of these parameters. However, there is a clear evidence that the scatter of the mass-bias distribution is larger for low-concentrated objects, high mass growth, and more generically for disturbed systems. Moreover, we carefully study the evolution of the bias of twelve clusters throughout a major-merger event. We find that the hydrostatic-mass bias follows a particular evolution track along the merger process: to an initial significant increase of the bias recorded at the begin of merger, a constant plateaus follows until the end of merge, when there is a dramatic decrease in the bias before the cluster finally become relaxed again. This large variation of the bias is in agreement with the large scatter of the hydrostatic bias for dynamical disturbed clusters. These objects should be avoided in cosmological studies because their exact relaxation phase is difficult to predict, hence their mass bias cannot be trivially accounted for.

Key words: methods: numerical – galaxies: clusters: general – galaxies: clusters: intracluster medium – large-scale structure of Universe.

1 INTRODUCTION

Galaxy clusters are the most massive gravitationally-bound structures in the Universe and, as such, their mass plays a key role in the estimation of the cosmological parameters. The majority of their mass is composed by Dark Matter (DM, almost 80%), the remaining part is composed by stars (galaxies) and hot gas which is diffused between the galaxies and it is called Intra-Cluster Medium, ICM (see Kravtsov & Borgani 2012, for a review).

The mass of these objects in observations can be estimated in several ways: from galaxy kinematic, applying the virial theorem to the distribution of cluster galaxies (for example Li et al. 2021), or directly from the velocity distribution of cluster galaxies (Zwicky 1937; Pratt et al. 2019; Tian et al. 2021; Hernández-Lang et al. 2022); from scaling laws, linking their total mass to several observable quantities, like X-rays luminosity or SZ (Sunyaev-Zeldovich) brightness (Nagarajan et al. 2018; Bulbul et al. 2019); from weak lensing (Von der Linden et al. 2014; Hoekstra et al. 2015; Okabe & Smith 2016; Artis et al. 2022) and, recently, also combining the

mentioned methods and using machine learning (Ntampaka et al. 2015; De Andres et al. 2022). Another frequently used approach is to derive the cluster mass under the assumption of the hydrostatic equilibrium (HE). This method uses temperature, density and pressure profiles of hot gas extracted from X-rays alone or combined with SZ effect observations (see Pratt et al. 2019 for a recent review). Three assumptions are the basis of the HE: the ICM must trace the cluster potential well, it must be spherically symmetric, and its pressure must be purely thermal. As shown in a recent review by Gianfagna et al. (2021), the HE mass evaluated in simulated samples is on average underestimating the true mass. In this paper we investigate more this subject and in particular the dependence of the bias by several other parameters that characterise the cluster dynamical state.

Numerical simulation studies find that the bias has a negligible dependence with the redshift (Piffaretti & Valdarnini 2008; Le Brun et al. 2017; Henson et al. 2017; Gianfagna et al. 2021). On the contrary, observational data are consistent with a decreasing mass bias along the redshift, see for instance Salvati et al. (2019) and Wicker et al. (2022) on *Planck* clusters. This dependence could be linked to a mass dependence of the bias, as clusters observed at higher redshifts tend to have a higher mass. However, the mass dependence is not

★ E-mail:

detected in simulations, either using the spectroscopic-like weighted temperature¹ (Mazzotta et al. 2004) to estimate the HE mass (Piffaretti & Valdarnini 2008; Le Brun et al. 2017; Henson et al. 2017; Pearce et al. 2019; Ansarifard et al. 2020; Barnes et al. 2021) or the mass-weighted temperature. Several authors also study the dependence of the bias on the dynamical state, the general findings also pointed towards no correlation, even if there is a hint that disturbed objects have a large scatter with respect to the relaxed ones (Piffaretti & Valdarnini 2008; Rasia et al. 2012; Nelson et al. 2014; Henson et al. 2017; Ansarifard et al. 2020). By comparing results in literature it appears that the hydrostatic mass bias does not depend on various cosmological-simulation ingredients, such as the baryon physics included in the simulations, the mass particles resolution or the number of objects in the samples (Gianfagna et al. 2021). Due to this consistency for simulated results, the discrepancy on the bias dependence on redshift between simulation predictions and observation results is still puzzling. This could be due to less numerous observational samples, due to a different mass sampling at high redshift and due to the uncertainty in the total physical mass estimation in observation.

The selection may also play a key role, for example the inclusion of disturbed objects. Indeed, all of the HE assumptions are violated during major mergers events which can induce strong dynamical perturbations, adding non-thermal support to the equilibrium budget (Nelson et al. 2012; Rasia et al. 2012, 2013; Angelinelli et al. 2020; Sereno et al. 2021). Therefore, the hydrostatic bias can significantly deviate from the expectation. In post-merger situations, then the merging object might have already been destroyed and thus it cannot be distinguished as a separate structure. Applying the hydrostatic-equilibrium technique to these cases (assuming they are in a relaxed state) will lead to a misinterpretation. Studying the extreme cases in simulations, where the dynamical state is clearly identified, will allow us to better understand the situations when the HE assumption is strongly violated and how the HE mass bias is impacted by mergers.

The organisation of this paper is as follow: in Section 2 we introduce THE THREE HUNDRED set of galaxy clusters, in Section 3 we give an overview on the hydrostatic equilibrium method. In Section 4 the ICM radial profiles are introduced, along with their analysis, and we introduce the parameters which will be used to characterise the dynamical state, the accretion and the geometry of clusters. In Section 5 we provide our the results, and we conclude in Section 6.

2 THE THREE HUNDRED PROJECT

This work is based on clusters simulated for THE THREE HUNDRED Project, introduced in Cui et al. (2018). This project is based on the resimulations of a set of 324 Lagrangian regions extracted from the MultiDark Planck (MDPL2) dark-matter-only (DM) cosmological simulation (Klypin et al. 2016) with different simulation codes. MDPL2 consists of a periodic cube of comoving length $1h^{-1}$ Gpc and 3840^3 N-body particles. The Lagrangian regions are identified at $z = 0$ around the most massive objects found in the parent simulation with a comoving radius of $15h^{-1}$ Mpc. The particles in those massive clusters and in their surrounding were traced back to $z = 120$ to generate the initial conditions for the zoomed-in re-simulations. The original mass resolution was kept in the central region, and those particles were split into dark matter and gas particles based

Table 1. The redshifts analysed in this work are written in the first column. The number of objects are in the second column. In the third, fourth and fifth columns are the mean masses at the three nominal overdensities 2500, 500, 200 with units of $10^{14}M_{\odot}$.

z	N	$\langle M_{2500} \rangle$ [$10^{14}M_{\odot}$]	$\langle M_{500} \rangle$ [$10^{14}M_{\odot}$]	$\langle M_{200} \rangle$ [$10^{14}M_{\odot}$]
1.32	277	0.47	1.36	1.99
1.22	281	0.55	1.58	2.31
0.99	304	0.78	2.26	3.29
0.78	305	1.07	3.04	4.45
0.59	305	1.48	4.05	5.91
0.46	300	1.73	4.89	7.22
0.33	297	2.09	5.73	8.46
0.22	298	2.43	6.73	9.97
0.07	290	2.98	8.19	12.20

on the cosmological baryon fraction Ω_b . The high-resolution dark-matter-particle mass is $1.87 \times 10^9 M_{\odot}$, while the initial gas mass is $3.48 \times 10^8 M_{\odot}$. In the outer region, the dark matter particles were degraded with multiple levels of mass refinements in several concentric shells. The 324 zoomed-in regions have been hydro-dynamically re-simulated with three different baryon models: GADGET-X (Rasia et al. 2015), GADGET-MUSIC (Sembolini et al. 2013) and GIZMO-Simba (Davé et al. 2019; Cui et al. 2022). In this work we use the GADGET-X simulated clusters. This code includes several radiative processes, like gas cooling, star formation, thermal feedback from supernovae, chemical evolution and enrichment, super massive black holes with AGN feedback (see Cui et al. 2018, for details).

The simulations assume a standard cosmological model according to the Planck Collaboration et al. (2016) results: $h = 0.6777$ for the reduced Hubble parameter, $n = 0.96$ for the primordial spectral index, $\sigma_8 = 0.8228$ for the amplitude of the mass density fluctuations in a sphere of $8h^{-1}$ Mpc comoving radius, $\Omega_{\Lambda} = 0.692885$, $\Omega_m = 0.307115$, and $\Omega_b = 0.048206$ respectively for the density parameters of dark energy, dark matter, and baryonic matter.

2.1 Sample

For the analysis presented here, we select the most massive cluster for each region that does not include any low-resolution particles within its virial radius. The evolution of the bias is tested at 9 redshifts, covering the redshift range between $z = 0.07$ and $z = 1.32$. The mean mass and the number of objects considered at each redshift are reported in Table 1 for the three studied overdensities: $\Delta = 2500$, 500 and 200. These indicate the radius R_{Δ} of a sphere whose density is either 2500, 500 or 200 times the critical density of the Universe at the consider cosmic time:

$$\rho_{\text{crit}} = (3/8\pi G)H_0^2[\Omega_M(1+z)^3 + \Omega_{\Lambda}], \quad (1)$$

where H_0 is the Hubble constant and G the gravitational constant.

3 THE HYDROSTATIC EQUILIBRIUM MASS

As said in the introduction, the hydrostatic equilibrium hypothesis is often at the basis of the procedure that lead to estimate the mass of galaxy clusters from X-ray observations (Kravtsov & Borgani 2012; Ettori et al. 2013). This assumption foresees that the gas thermal pressure, which naturally leads to expansion of the gas, is balanced by the gravitational forces, which, on the other side, causes the systems

¹ Note that spectroscopic-like weighted temperature is more similar to the X-ray temperature obtained from X-ray spectroscopic analysis of observed data.

to collapse. The equilibrium is expressed as the equality between the gradient of the thermal pressure and that of the gravitational potential and it is supposed to hold at every concentric distance from the cluster centre. Connecting the gravitational potential to the mass, under the spherical assumption, leads to the following formula for the total mass inside a sphere of radius r :

$$M_{\text{HE,SZ}}(< r) = -\frac{r^2}{G\rho_g(r)} \frac{dP_{\text{th}}(r)}{dr} \quad (2)$$

where ρ_g and P_{th} are the density and the thermal pressure of the gas, respectively. We will refer to this mass as $M_{\text{HE,SZ}}$, since the radial pressure profile can be derived from Compton- y parameter maps provided by clusters SZ observations at millimetre wavelengths.

Assuming the equation of state of an ideal gas, the cluster mass can also be estimated with gas density and temperature separately:

$$M_{\text{HE,X}}(< r) = -\frac{rk_{\text{B}}T(r)}{G\mu m_{\text{p}}} \left[\frac{d \ln \rho_g(r)}{d \ln r} + \frac{d \ln T(r)}{d \ln r} \right]. \quad (3)$$

We refer to this HE mass formulation as $M_{\text{HE,X}}$ because historically this expression was used in the analysis of X-rays observations (Ansarifard et al. 2020). The detailed computation of the HE mass in our simulated sample will be introduced in next section.

This mass is compared with the true total mass of the systems, obtained by summing over all dark matter, stars and gas particle masses inside a fixed aperture radius. The mass bias b_{SZ} or b_{X} is defined as

$$b = \frac{M_{\text{true}} - M_{\text{HE}}}{M_{\text{true}}}. \quad (4)$$

This bias can be either positive, when the HE mass is underestimating the true cluster mass, or negative, when there is an overestimation of the true mass. A null bias results in a perfect estimate of the true mass through HE.

4 METHODS

In this work, we aim to estimate the two hydrostatic masses, as presented in Eqs. (2) and (3). The ICM temperature, gas density and pressure radial profiles play a fundamental role in the calculation of these masses. In this section, we describe how we compute them in THE THREE HUNDRED simulations together with other relevant quantities which we use to study the correlations with the bias. The quantities linked to the study of the mass bias during a major merger event will be described in Section 5.2.

4.1 The ICM profiles

The cluster profiles are extracted in logarithmically equal-spaced radial bins, centred at the maximum density (mostly coinciding with the minimum of the potential well, see also Cui et al. 2016; Ansarifard et al. 2020). Only gas particles with density below the star-formation density threshold and with temperature above 0.3 keV are considered as ICM for calculation, this is to insure that we are selecting the hot particles which can generate X-ray or SZ signals, in order to match the observations.

Once the profiles are extracted, we fit them with analytic models which will be described below. We then use the analytical best-fitting curves to estimate the hydrostatic masses. Following this strategy will allow to avoid the small fluctuations that are presented in the 3D numerical profiles which strongly impact the calculation of the derivatives in the hydrostatic-equilibrium mass equations (see Giannafagna et al. 2021). On average, this still allow to well fit the large

Table 2. The medians and 16th – 84th percentiles of best-fit free parameters in Eq. 5 for gas density profiles and the reduced χ^2 . The results only for all $z = 0.07$ clusters are exhibited here. The c parameter is fixed to 3.

$\rho_0 [10^{13} \text{M}_{\odot}/\text{Mpc}^3]$	$r_d [\text{Mpc}]$	$r_s [\text{Mpc}]$	a
$3.5^{+1.5}_{-1.3}$	$0.71^{+0.20}_{-0.17}$	$0.73^{+0.65}_{-0.29}$	$1.2^{+1.2}_{-0.9}$
b	e	$\rho_{0,2} [10^{13} \text{M}_{\odot}/\text{Mpc}^3]$	$r_{d,2} [\text{Mpc}]$
$2.6^{+0.4}_{-0.7}$	$2.5^{+0.4}_{-0.6}$	$2.4^{+0.6}_{-0.8}$	$0.95^{+0.36}_{-0.28}$
b_2	χ^2		
$1.2^{+0.3}_{-0.2}$	$1.1^{+0.8}_{-0.4}$		

fluctuations (bumps or deeps in the profiles), caused by substructures, which should instead taken into account. This is valid especially for the temperature and density models, that have the largest number of parameters. The pressure profile model could instead cancel some large fluctuation, due to the smaller number of parameters, leading to a non-reliable SZ bias, but the two biases are compatible between each other (see Section 5) and also the scatter is not significantly different. The best-fit procedure of each profile is performed in the radial range $[0.2-3]R_{500}$. This range was chosen to include the three studied overdensities: $\Delta = 2500, 500$ and 200 . We study the goodness of the fits using the χ^2 test and found that all the fits can be classified as good fits.

4.1.1 Gas Density

The 3D gas density profiles are estimated as the total gas mass in a spherical shell, divided by the shell volume: $\rho = \sum m_i / V_{\text{shell}}$. The model chosen to fit this profile is the one proposed by Vikhlinin et al. (2006):

$$\rho_g(r) = \rho_0^2 \frac{(r/r_d)^{-a}}{(1 + (r/r_d)^2)^{3b-a/2}} \frac{1}{(1 + (r/r_s)^c)^{e/c}} + \frac{\rho_{02}^2}{(1 + (r/r_{d2})^2)^{3b_2}}, \quad (5)$$

where we fix the parameter c equal to 3 and we impose the following limitation: $e < 5$. The other 8 parameters are left free. Often in literature this model is simplified by discarding the second beta model, here we keep it to have a reliable fit also in the cluster region near R_{2500} . For reference, we report in Table 2 the medians of all best-fit parameters computed from the sample at $z = 0.07$.

4.1.2 Gas Temperature

The mass-weighted temperature profile is estimated as a weighted average over the gas particles in the same spherical shells used for the gas density:

$$T = \frac{\sum_i (m_i T_i)}{\sum_i m_i}. \quad (6)$$

where m_i and T_i are the mass and temperature of i^{th} gas particle. Using the mass-weighted temperature is the optimal choice for hydrostatic equilibrium studies which theoretically connect the temperature with the gravitational mass (Biffi et al. 2014) and it is favorable with respect to the spectroscopic-like temperature (Mazzotta et al. 2004). The analytical model for the mass-weighted temperature used

Table 3. The medians and 16th and 84th percentiles of best-fit free parameters of Eq.7 and the reduced χ^2 computed for all $z = 0.07$ clusters.

T_0 [keV]	τ	r_t [Mpc]	α	β	γ
15.3 ^{+56.4} _{-10.3}	0.37 ^{+0.32} _{-0.33}	2.3 ^{+22.6} _{-1.29}	0.29 ^{+0.71} _{-0.29}	4.6 ^{+7.4} _{-4.6}	1.3 ^{+2.2} _{-1.3}
r_{cool} [Mpc]	α_{cool}	χ^2			
1.4 ^{+1.5} _{-0.7}	5.4 ^{+4.6} _{-2.8}	1.4 ^{+0.4} _{-0.1}			

Table 4. The medians and 16th and 84th percentiles of best-fit free parameters of Eq.8 and the reduced χ^2 computed for all $z = 0.07$ clusters. The i parameter is fixed equal to 0.31.

P_0 [10 ⁻² keV/cm ³]	r_s [Mpc]	g	h	χ^2
2.6 ^{+5.5} _{-1.5}	3.1 ^{+6.9} _{-2.5}	1.1 ^{+1.3} _{-0.4}	8.2 ^{+6.8} _{-4.0}	1.1 ^{+0.8} _{-0.3}

in this work was introduced again by [Vikhlinin et al. \(2006\)](#):

$$T(r) = T_0 \frac{x + \tau}{x + 1} \frac{(r/r_t)^{-\alpha}}{(1 + (r/r_t)\beta)^{\gamma/\beta}}, \quad (7)$$

$$x = (r/r_{cool})^{\alpha_{cool}}.$$

All the 8 parameters are free to vary. Their medians for the $z = 0.07$ clusters are reported in Table 3.

4.1.3 Gas Pressure

The radial thermal pressure profile is measured from the gas density and temperature of each gas particle. It is modelled by the generalised Navarro-Frenk-White (gNFW) model ([Nagai et al. 2007](#)):

$$P(r) = \frac{P_0}{x^i (1 + x^g)^{\frac{h-i}{g}}}, \quad (8)$$

where $x = r/r_s$ is a dimensionless radial distance normalised to the scale radius, r_s . The parameters h and i are the slopes for outer and inner region, respectively, and g is the steepness of the transition between the two regimes. This model has 4 free parameters, since $i = 0.31$ is fixed ([Arnaud et al. 2010](#)). The medians of the best-fit parameters for the $z = 0.07$ sample are listed in Table 4.

4.2 The NFW concentration

Similarly to the thermodynamical profiles, we compute the total density profiles which include the contribution from all particles in the simulations (dark matter, gas, stars). The total mass profile is fitted with a NFW model ([Navarro et al. 1997](#)):

$$M(< r) = M_0 \left[\log(1 + x) - \frac{x}{1 + x} \right]. \quad (9)$$

As before the radial coordinate is related to the scale radius, $x = r/r_s$. This parameter, together with the normalisation, is derived from a best-fitting procedure applied in the radial range between 100 kpc and R_{200} , which roughly reproduce a typical radial range used in weak-lensing analysis. The concentration within R_{500} is defined from the scale radius: $c_{500} = R_{500}/r_s$.

4.3 Relative mass growth

We straightforwardly define the cluster mass growth as the relative mass difference between an initial, t_1 , and a final time, t_2 :

$$\frac{\Delta M/M}{dt} = \frac{(M(t_2) - M(t_1))/M(t_1)}{[t_2 - t_1]}. \quad (10)$$

Specifically, we estimated the mass growth from the merger tree between $z_2 = 0.33$ and $z_1 = 0.46$, so that $t_2 - t_1$ corresponds to about 1 Gyr (precisely it is equal to 1.046 Gyr). This interval corresponds to 5 simulation snapshots.

4.4 Dynamical state parameter

The dynamical state of the clusters has been inferred by the combination of two indicators computed in 3D ([Neto et al. 2007](#); [Cui et al. 2017](#); [Cialone et al. 2018](#); [De Luca et al. 2021](#)):

- $f_s = M_{\text{sub}}/M_{\Delta}$, which is the fraction of cluster mass included in substructures inside a fixed overdensity;
- $\Delta_r = |\mathbf{r}_{\delta} - \mathbf{r}_{\text{cm}}|/R_{\Delta}$, which is the offset between the positions of the maximum density peak and the centre of mass of the cluster within R_{Δ} and normalised to that aperture radius.

When correlating the dynamical-state and the HE mass bias, we evaluate all quantities of interest at the same overdensity value. In order to have a relaxed cluster, both indicators should be smaller than 0.1 ([Cialone et al. 2018](#)) while they should be both greater than 0.1 to have a disturbed one. The other cases are classified as intermediate or hybrid. The percentage of relaxed clusters is almost 50% at low redshifts, and decreases to 30% at high redshifts, while the percentage of disturbed clusters is 20% at low redshifts and increases to 30% at high redshifts ([De Luca et al. 2021](#)). As previously said, in our study we consider one combined parameter as in [Haggar et al. \(2020\)](#) but derived exclusively from the two mentioned indicators as in [De Luca et al. \(2021\)](#):

$$\chi_{\text{DS}} = \sqrt{\frac{2}{\left(\frac{\Delta_r}{0.1}\right)^2 + \left(\frac{f_s}{0.1}\right)^2}}. \quad (11)$$

Using the χ_{DS} parameter is a continuous way to classify the state of the cluster where the relaxed ones satisfy $\chi_{\text{DS}} > 1$. We use this parameter to study the dependence of the dynamical state on the HE bias (see Section 5.1.4). An extensive study of the relaxation state of THE THREE HUNDRED clusters including its dependence from redshift is presented in [De Luca et al. \(2021\)](#).

4.5 Triaxiality

In order to test how much the lack of spherical symmetry is affecting the HE mass estimate, we calculate, using all particles within R_{500} , the three axes of the inertia tensor as in ([Vega-Ferrero et al. 2017](#)). We then use the ratio c/a and the triaxiality of the halos:

$$t = \frac{1 - (b/a)^2}{1 - (c/a)^2}, \quad (12)$$

where a , b and c indicate the major, intermediate, and minor axes, respectively. Depending on the value of the parameter t , the halo is considered as oblate if $0 < t < 1/3$; triaxial if $1/3 < t < 2/3$ and prolate if $2/3 < t < 1$. More simply, when c/a is equal to 1 the cluster is spherical.

5 RESULTS

In this section we present the results of our work. First, in Section 5.1, we study the HE mass bias dependencies on the redshift, mass, and on all other parameters: the concentration, the mass growth, the relaxation parameter and the triaxiality. We performed all these analyses at the three overdensities ($\Delta = 2500, 500, 200$) and at all considered redshifts. However, most of the figures related to this part of the work (with the exception of the first) are only presented with $\Delta = 500$ and at one specific redshift because we do not find a strong dependence of the results on either of these two quantities.

Secondly, in Section 5.2, we analyse how the HE mass bias varies throughout strong merger events. In this case, we only analyse the behaviour of the bias at R_{200} , since we take as reference the mergers analysis in Contreras-Santos et al. (2022), which is done considering the entire cluster volume and thus at overdensity 200.

5.1 Bias correlations

5.1.1 Redshift dependence

The variation of b_{SZ} and b_X along the redshift range is presented in Fig. 1 at the 3 overdensities and for the different cluster dynamical states defined with the dynamical-state parameter, χ_{DS} . For all overdensities, the un-relaxed clusters (purple shaded region) have the largest scatter. Interestingly, this large scatter is mostly caused by the presence of low-value bias. We will present the reason in Section 5.2. No dependence of the bias on the redshift up to $z = 1.25$ is detected in agreement with Le Brun et al. 2017; Henson et al. 2017; Salvati et al. 2018; Koukoufilippas et al. 2020. Furthermore, we notice that the median b_{2500} is very similar to the median b_{500} and that both are close to 0.1 (10% of bias) and as such systematically lower than b_{200} (close to ~ 0.2). This is in agreement with Gianfagna et al. (2021), which showed a declining b from outer to inner radius. This is occurring despite the differences both in the code (GADGET2 versus GADGET-X) and in the baryon models. Note, however, that the SZ and X median b_{500} in Gianfagna et al. (2021) is slightly larger than this work. The biases dispersion at R_{2500} seems to be slightly larger with respect to the other overdensities, this is probably due to the larger deviations in the cluster core properties, which could marginally affect the profile at R_{2500} . In THE THREE HUNDRED, the simulation produce a more diverse variety of simulated cores with respect to the GADGET2 code, and in some situations, the simulated clusters are extremely peaked at the centre (see Campitiello et al. 2022).

5.1.2 Concentration

The concentration parameter c_{500} of a halo is representative of the halo's central density. In presence of a disturbed system the concentration is typically lower since the X-ray peak might have been destroyed by a merger event which also could have brought more mass in the external regions. For this it might be interesting to see if there is any correlation between the HE mass bias and the NFW concentration parameter.

The bias as a function of the concentration is represented in Fig. 2 where the relaxed, disturbed and hybrid clusters are introduced with different symbols and colours. Hybrid clusters are these with either $f_s < 0.1$ or $\Delta_r < 0.1$. The two quantities do not show any dependence, as clear from the trend of the median value shown with a black line. We notice however that the scatter in the bias substantially decreases going towards larger concentration values.

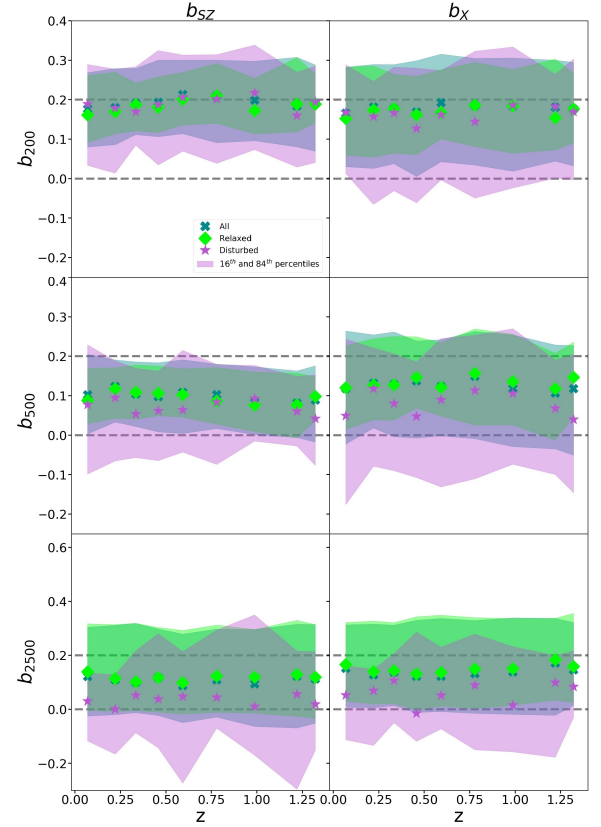


Figure 1. The redshift evolution of the biases, b_{SZ} (left panels) and b_X (right panels). The median values of the bias for all clusters, relaxed and un-relaxed clusters are represented with dark cyan crosses, green diamonds and purple stars respectively. The shaded regions represent the 16th and 84th percentiles. The bias estimated at R_{200} , R_{500} and R_{2500} are represented in the top, middle and bottom panels respectively. The dashed lines show the 0 and 0.2 bias for reference.

Table 5. Table of the biases for the 50 clusters with the highest (first row) and lowest (third row) NFW concentration and the remaining clusters (second row) for the $z = 0.59$ sample. We report the median value (m), the 16th and 84th percentiles (p_{16} and p_{84}), and their half difference (d_2) at R_{500} .

c_{500}	b_{SZ}				b_X			
	m	p_{16}	p_{84}	d_2	m	p_{16}	p_{84}	d_2
high	0.11	0.07	0.19	0.06	0.12	0.05	0.24	0.10
med	0.11	0.00	0.18	0.09	0.13	0.00	0.24	0.12
low	0.06	-0.03	0.22	0.12	0.11	-0.07	0.24	0.15

This is quantified by the half difference between the 16th and the 84th percentiles, $d_2 = 0.5 \times (p_{84} - p_{16})$ reported in Table 5 together with the bias percentiles. The value of d_2 decreases from low (third row) to high concentrated clusters (first row) by 70-80%. This trend – reduced scatter with increasing concentration – is expected because most of the clusters with higher concentration are relaxed.

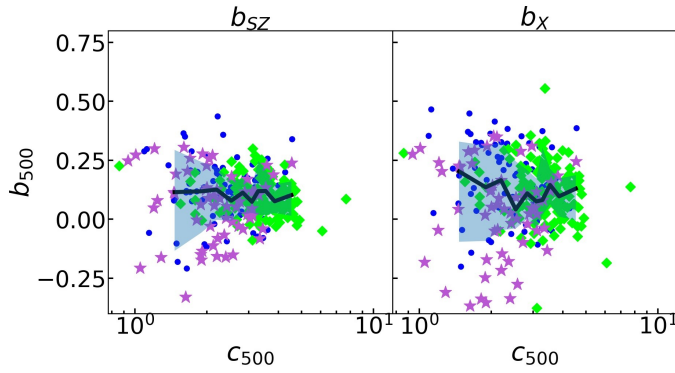


Figure 2. The bias dependence on the concentration at R_{500} and at $z = 0.07$, b_{SZ} is represented in the left panel, b_X in the right one. The black line represents the median bias value, with the shaded regions as 16th and 84th percentiles. The relaxed clusters are shown in green diamonds, the disturbed in purple stars and the hybrids in blue dots.

5.1.3 Relative Mass growth

The dependence of the bias at $z = 0.333$ on the mass growth recorded in the last Gyr (and specifically since $z = 0.46$) is shown in the top panel of Fig. 3, where both quantities are estimated at R_{500} . The relative median values for high, low, and intermediate accreting clusters are listed in Table 6. The correlation is again very weak, the Pearson correlation coefficient is -0.20 for b_{SZ} and -0.36 for b_X . However, the systems with the largest mass growth have also the largest dispersion. This is expected because the systems with the largest mass growth are also the most disturbed (purple stars in Fig. 3). This relation will be discussed more afterwards, however, we point out that clusters with large mass accretion will also have abundant non-thermal gas motions and, thus, a large non-thermal pressure component. The same trend is seen for the quantities estimated at R_{200} , with a Pearson correlation coefficient of 0.16 for b_{SZ} and 0.21 for b_X .

In the bottom panel of Fig. 3 the difference between the bias at $z_2 = 0.33$ and at $z_1 = 0.46$ is shown ($\Delta b = b(z_2) - b(z_1)$). The variation in the bias for disturbed clusters (at large accretion rates) is negative, implying that the HE mass bias overall decreases. This phenomenon which might seem surprising will be better studied in Section 5.2, but we can already see from the top panel the origin of this trend: after a major merger (with a mass variation of at least 50% $\Delta M/M > 0.5$) the mass computed by Eqs. 2 or 3 can be significantly larger than the true mass with a large scatter as well (see also Nelson et al. 2012).

Overall Fig. 3 shows that the mass growth is a parameter that is capable to distinguish between relaxed and disturbed clusters, as seen also in Fig. 4. We, indeed, find a correlation between the mass growth parameter and χ_{DS} equal to -0.46 both at R_{500} (shown in the Figure) and at R_{200} . The good correlation is actually expected since one of the indicators defining χ_{DS} is the mass in substructures. That said there is a certain level of contamination with the presence of disturbed objects with reduced mass growth or viceversa relaxed objects with significant mass growth. Notice, however, that both these peculiar cases have a HE bias value which is quite consistent with the average expectation of the samples, while extreme bias values such as those with $b < -0.2$ are only present for the largest mass growth.

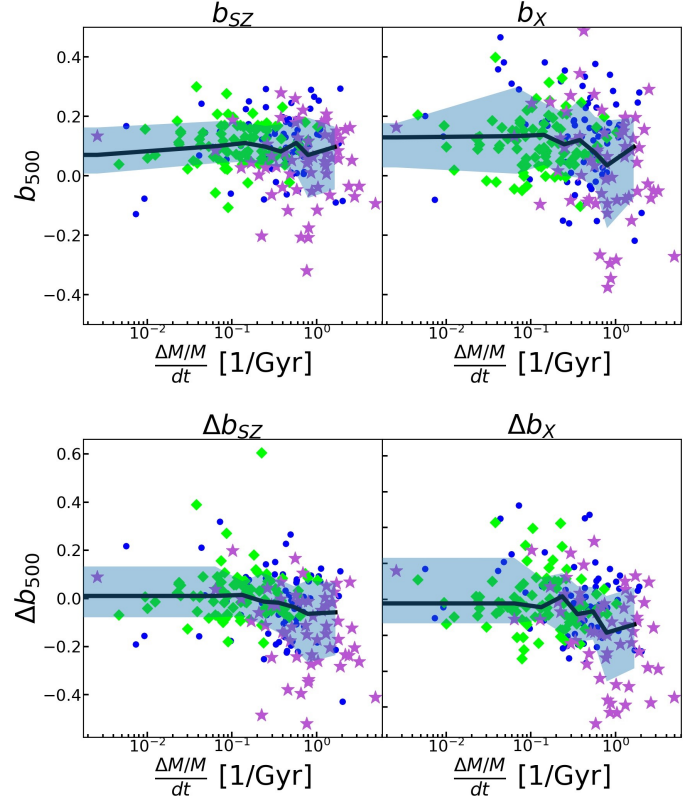


Figure 3. Top panel: the bias dependence on the mass growth $\frac{\Delta M}{dt}$ is represented. $\frac{\Delta M}{dt}$ is estimated from $z = 0.46$ to $z = 0.33$, which corresponds to 1 Gyr, while the biases are estimated at $z = 0.33$. Bottom panel: the bias variation from $z = 0.46$ to $z = 0.33$ as a function of $\frac{\Delta M}{dt}$. The relaxed and disturbed clusters are represented with green diamonds and purple stars respectively, while the hybrids with blue dots. The cluster dynamical states shown in this plot are estimated at $z = 0.33$.

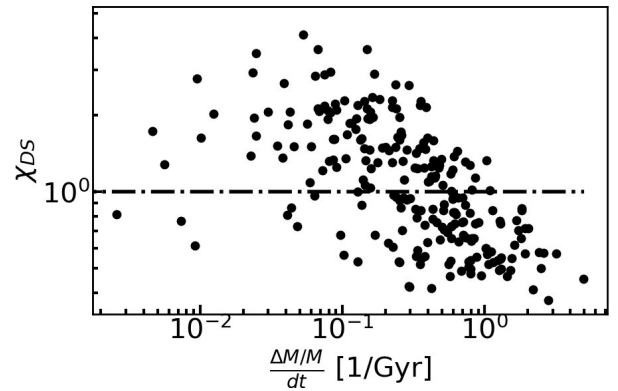


Figure 4. The relaxation parameter at $z = 0.33$ is represented as a function of the mass growth from $z = 0.46$ to $z = 0.33$, all estimated at R_{500} . The dot-dashed line represents the threshold under which a cluster is considered disturbed.

Table 6. Table of the biases values for the 50 clusters with the largest mass growth (first row), the 50 with the smallest (last row) and the remaining clusters (second row) for the $z = 0.33$ sample. We report the median value (m), the 16th and 84th percentiles (p_{16} and p_{84}), and their half difference (d_2) at R_{500} .

Mass growth	b_{SZ} m	p_{16}	p_{84}	d_2	b_X m	p_{16}	p_{84}	d_2
high	0.09	-0.05	0.17	0.11	0.09	-0.12	0.20	0.16
med	0.10	-0.02	0.17	0.08	0.12	0.00	0.22	0.11
low	0.14	0.06	0.22	0.08	0.24	0.10	0.35	0.13

Table 7. Table of the bias values for the 50 highest (first row) and 50 lowest (third row) χ_{DS} clusters and for the remaining clusters (second row) for the $z = 0.59$ sample. We report the median value (m), the 16th and 84th percentiles (p_{16} and p_{84}), and their half difference (d_2) at R_{500} .

χ_{DS}	b_{SZ} m	p_{16}	p_{84}	d_2	b_X m	p_{16}	p_{84}	d_2
high	0.10	0.05	0.16	0.06	0.12	0.05	0.23	0.09
med	0.11	-0.02	0.19	0.09	0.14	0.01	0.25	0.12
low	0.11	-0.04	0.21	0.13	0.07	-0.12	0.20	0.16

5.1.4 Relaxation parameter

The bias as a function of the relaxation parameter is represented in Fig. 5, where, per definition, the coloured points of relaxed and disturbed clusters are completely separated. Weak or no correlations is found, indeed the Pearson correlation coefficients with the highest values are only equal to 0.13 for b_{SZ} and 0.23 for b_X at $z = 1.32$; and 0.01 for b_{SZ} and 0.01 for b_X at $z = 0.07$. Also in this case, the disturbed clusters show a wider dispersion with respect to the relaxed ones, see Table 7, where the difference between the bias percentiles grows by almost a factor of 2 from the lowest to the largest χ_{DS} clusters. This is in agreement with Piffaretti & Valdarnini (2008); Rasia et al. (2012); Nelson et al. (2014); Henson et al. (2017); Ansarifard et al. (2020).

5.1.5 Total mass

We continue to investigate the correlation between the HE bias and the cluster mass at R_{500} in Fig. 6. Since we detect no variation on cosmic time (see Fig. 1), in this plot, we simultaneously show the biases at four redshifts (1.32, 0.78, 0.33, 0.07) to increase the halo mass range. We find no dependence of the bias on the total mass of the clusters in agreement with Piffaretti & Valdarnini (2008); Le Brun et al. (2017); Henson et al. (2017); Pearce et al. (2019); Ansarifard et al. (2020); Barnes et al. (2021).

5.1.6 Triaxiality

We study the dependence of the bias at R_{500} on the sphericity of the halos, one of the HE main assumptions, quantified with the parameter t and on c/a , the ratio of the minor and major axis. All the particles within R_{500} are used to estimate the halo shape (Vega-Ferrero et al. 2017).

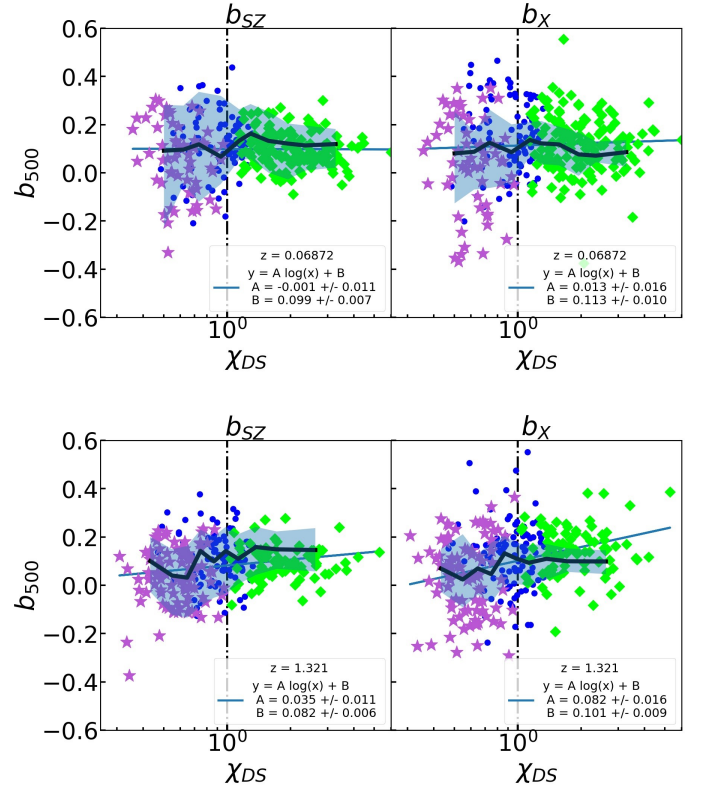


Figure 5. The biases are represented as a function of the relaxation parameter χ_{DS} . The hybrids, relaxed and disturbed clusters are represented with blue dots, green diamonds and purple stars respectively. In the top panel we show the quantities at $z = 0.07$ and in the bottom one at $z = 1.3$. The lines are the results of a simple linear fitting result. The black line and the shaded region represent the median bias and the percentiles (16th and 84th).

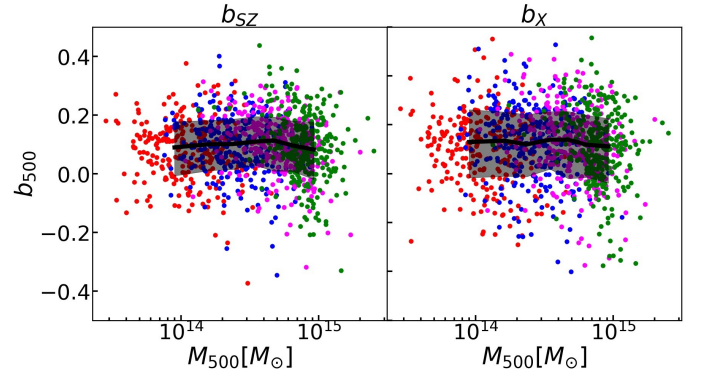


Figure 6. The biases are represented as a function of the cluster total mass, both at R_{500} . The redshifts 1.32, 0.78, 0.33, 0.07 are represented in red, blue, magenta and green, respectively. The black line and the shaded region represent the binned median and the 16th-84th percentiles.

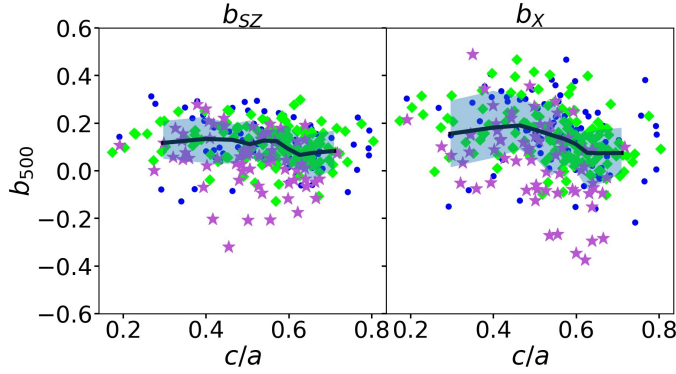


Figure 7. The biases at R_{500} are represented as a function of the axis ratio c/a . The hybrids, relaxed and disturbed are represented with blue dots, green diamonds and purple stars respectively. Both b_{SZ} and b_X are shown for $z = 0.33$. The median value of the bias is represented with the black line, the 16th and 84th percentiles with the shaded region.

Table 8. Table of the biases values for the 50 clusters with the highest (first row) and lowest (last row) axial ratio and for the remaining clusters (second row) for the $z = 0.46$ sample. We report the median value (m), the 16th and 84th percentiles (p_{16} and p_{84}), and their half difference (d_2) at R_{500} .

c/a	b_{SZ}				b_X			
	m	p_{16}	p_{84}	d_2	m	p_{16}	p_{84}	d_2
high	0.09	0.01	0.18	0.07	0.11	-0.00	0.18	0.09
med	0.09	0.00	0.17	0.08	0.14	-0.02	0.23	0.13
low	0.12	0.02	0.24	0.11	0.20	0.07	0.32	0.12

The relation between the biases and c/a is represented in Fig. 7, the results for t are not shown, being very similar. From that Figure we notice that the overall correlation and the amplitude of the scatter seem to be uncorrelated with the axial ratio. Although, if we restrict to the most aspherical cases (third line in Table 8) we see that the both biases increases by almost 50% with respect to the objects with the highest c/a values. Note that the halo shape estimated based on total mass is similar to the one based on hot gas (see Velliscig et al. 2015, for details). Therefore, we believe a similar result will be in place when the halo shape is estimated only from the gas particles.

5.2 HE mass bias and the merger history of the clusters

Unlike observations, hydrodynamical simulations allow for tracking the whole history of a cluster, and thus to follow a merging event during all its phases. Specifically in this subsection, we study major merger events that are identified when a halo experiences a very rapid mass increase, primarily caused by the accretion of a single massive object (Contreras-Santos et al. 2022). Our main goal is to understand the evolution of the bias throughout these violent merging processes.

To define and compute the relevant times to the merger event, we closely follow the definitions in Contreras-Santos et al. (2022) to which we refer for a more detailed explanations. In summary, instead of using absolute time as the variable in the merger history, which

can vary with redshift, we normalise it to the halo dynamical time:

$$t_{dyn} = \sqrt{\frac{3}{4\pi} \frac{1}{200G\rho_{crit}}}. \quad (13)$$

Since the critical density depends only on the cosmology and on the redshift, see Eq. (1), the dynamical time does not depend on the cluster features, but evolves only with redshift. As described before, we only consider the major merger events defined as an event that produces a mass increase of 100% within half of the dynamical time

$$\frac{\Delta M}{M} = \frac{M_f - M_i}{M_i} \geq 1, \quad (14)$$

where M_i is the initial mass and M_f is the final mass. Note that the masses in this case refer to the overdensity of 200. We use this larger radius for better capturing the evolution process inside the virial region. The merger event can easily be characterised by 4 particular redshifts (see Figure 1 of Contreras-Santos et al. 2022):

- z_{before} : the last time before the merger begins. It is characterised by a relaxation parameter with high values (typically larger than 1). Soon after the two systems start to influence each other and the relaxation parameter decreases;
- z_{start} : the merging halo enters in the main cluster R_{200} and as a consequence the mass of the latter starts to grow;
- z_{end} : the end point of the merger identified as the moment when the mass growth stops and the χ_{DS} starts to grow again implying that the relaxation process is beginning.
- z_{after} : the end of the whole merger phase when the cluster approaches a relaxed state by showing χ_{DS} closer or above 1.

In this work, we analyse how the bias evolves with the major merger event and how much time is needed for the bias to return to the average value in the relaxed population. In our sample, we select 12 clusters which experience a major merger, from z_{before} to z_{after} , in the investigated redshift range [0.07, 1.32]. In the top panel of Fig. 8 the two stacked biases, presented by mean bias values with 16th – 84th percentiles as error bars, are shown as a function of $\Delta t/t_{dyn}$, which is defined as

$$\frac{\Delta t}{t_{dyn}} = \frac{t_{0+i} - t_0}{t_{dyn}} \quad (15)$$

where t_0 corresponds to the analysed redshift right before z_{before} , and t_{0+i} corresponds to the analysed redshifts following t_0 . The vertical grey shaded areas represent the $\pm 1\sigma$ regions of the averaged time before, after, start and end of the merger. The yellow shaded region shows the $\pm 1\sigma$ region of the SZ bias for the relaxed clusters at R_{200} , averaged over all the redshifts.

At $\Delta t/t_{dyn} = 0$ both biases are in agreement with the typical relaxed clusters values. Right at the beginning of the merger phase (z_{before}), the biases increase to $\sim 0.25 - 0.3$ due to the incoming substructure, that causes the true mass of the cluster to increase faster than the HE mass, leading to a slight increase of the bias. The latter stays almost constant until the end of the accretion of the secondary object. In this situation the HE mass is always underestimating the true mass of the object. A small increase of the bias is detected at around z_{end} followed by a quick decrease that lasts until z_{after} , where a minimum is reached. Right at this time, around the end of the merger phase, the HE bias can even reach negative values. The in-fall of the substructure generates shocks propagating outward. These shocks cause a steep increase of the derivatives of the pressure, gas density and temperature profiles (see the bottom panel described later), leading to an increase of the HE mass, and a negative bias.

This trend is in agreement with [Bennett & Sijacki \(2022\)](#) and [Nelson et al. \(2012\)](#), who conducted a similar study on simulated clusters. When the cluster approaches a relaxation phase at $\sim z_{\text{after}}$, the bias returns to a value that is closer to the mean b of relaxed clusters. This trend is again in agreement with what seen in the FABLE simulated clusters ([Bennett & Sijacki 2022](#)).

In the middle panel of Fig. 8 we show the evolution of the relaxation parameter during the merger process. The clusters are classified as relaxed at t_0 by definition, and then as the secondary cluster approaches (before z_{start}) the χ_{DS} drops. The relaxation parameter shows some fluctuation between z_{start} and z_{end} to finally grow again after the secondary objects is completely incorporated into the main cluster. At the end of the merger phase (z_{after}), per definition χ_{DS} is approaching 1. Notice that even after 4 dynamical times from the beginning of the merger the main cluster does not reach the original relaxation state, consistently with [Contreras-Santos et al. \(2022\)](#).

In the bottom panel, we show the relative evolution of all quantities entering the HE mass equations (both thermodynamic quantities and their derivatives). To be consistent with the analysis shown in the upper panels, all the values are computed at R_{200} . The pressure derivative is represented with blue triangles, the temperature and its derivative are represented as olive green dots and triangles, the gas density and its derivative are represented with orange dots and triangles. The temperature derivative does not show any particular trend and fluctuates around the original values with large error bars. The temperature values instead grows immediately as the secondary object approaches and keeps growing until the end of the process, this is expected as it is a consequence of the shock heating produced by the merger.

The density value does not show any particular change until the secondary structure merge into the main halo after z_{start} . The slope of the gas density at R_{200} also increases for the presence of the massive companion. In both cases, the variation continues up to z_{end} before reaching a plateau. Finally, the pressure derivative is on the mid way between the temperature and the gas density derivatives. The increase in the derivative of the gas density, pressure and temperature due to the shocks generated in the merger or to the sloshing of the subclusters moving around the cluster core drive the HE masses of Eqs. 2 and 3 to be closer or even above the true mass.

At R_{500} these considerations are still valid, the behaviour of all the quantities is the same. To conclude, the bias shows a stable evolution along the whole major merger event, albeit slightly difference between b_{SZ} and b_{X} . However, the dramatic change of the bias value, especially in the period between z_{end} to z_{after} when the cluster is identified as un-relaxed, is the origin of the large scatter of the bias for the disturbed systems shown in all previous figures. For this reason, it is not suggested to estimate the HE masses for these dynamical un-relaxed clusters, unless we can correctly identify their states in the merging events which can be very difficult in observation.

6 CONCLUSIONS

Galaxy cluster mass plays a major role in cluster cosmology. Several different methods are used to estimate it. In this paper we focus on the hydrostatic equilibrium approximation, which makes use of the temperature, pressure and density radial profiles of the ICM. These 3D profiles are computed from THE THREE HUNDRED simulations, which include a set of almost 300 simulated galaxy clusters that we studied at 10 different redshifts. From the profiles, we recover the masses under the HE approximation and we estimate the bias against the true cluster total mass. In this work the focus is specifically on the

connection between the hydrostatic mass bias and different cluster properties, such as dynamical state, cluster total mass, mass-growth rate, NFW concentration and axial ratio. Moreover, we follow the bias during 12 major-merger events to understand the bias evolution along these events. The main findings are as follows:

- We do not find correlation between the biases, estimated at different radii, and the redshift, in agreement with other simulations.
- The bias and its scatter are influenced by the radii within which the bias is estimated, i.e. R_{2500} , R_{500} and R_{200} in this work. The largest bias is at R_{200} (almost 20%), while at R_{500} and R_{2500} , the median value is around 10%.
- There is no correlation between the hydrostatic mass bias and the dynamical state of the clusters as measured with different indicators: the dynamical-state parameter χ_{DS} , the NFW concentration, the relative mass growth, and the triaxiality. However, whenever one of these parameters is typically associated to a disturbed objects (e.g. low χ_{DS} , low concentration, high mass growth) we detect a bias scatter that can be almost twice as that of the relaxed systems. The scatter has, instead, little dependence on mass, redshift, and sphericity.
- A moderate correlation is found between the relaxation parameter and the mass growth. This is expected because the larger is the mass growth, the more likely the cluster is disturbed.
- By stacking clusters while experiencing major merger events we find that the main object becomes more disturbed along the merger with a slightly higher b , when the secondary structure collides. After z_{end} – the halo mass growth stops and b drops significantly because of the shocks propagating outward generated by the in-falling substructure. These shocks cause a steep increase of the derivatives of the pressure, gas density and temperature profiles, even leading to an overestimation of the HE mass. At the end of the merger phase when clusters get closer to a relaxed dynamical state with $\chi \sim 1$, the bias assumes the typical values of relaxed clusters.

Although no correlation is found between the HE bias and the dynamical state of the cluster at a given redshift, we find that selecting a sample with the typical characteristics of regular objects, such as high NFW concentration, low mass accretion rate, high χ_{DS} , and high c/a ratio, leads to a reduced cluster-to-cluster scatter. We also found a correlation between various merger phases and the HE bias which can be close to 0 when the cluster is at the end of merger process. This, however, occurs when the cluster is not yet relaxed confirming that including yet-no relaxed clusters could largely increase the bias scatter.

Our results are in agreement with other simulations, where a large bias is found mostly generated by deviations from spherical symmetry (which is at the base of HE), temperature dishomogeneities, but also the presence of substructures or gas motions, generating non-thermal pressure component. In the first part of the paper, we have proved that the HE bias is not dependent on the latter, while in the last part of the paper we explore how the bias changes during a merger. Here we show that the presence of a substructure, and consequently a merger, can indeed deeply affect the cluster dynamical state and the HE mass bias, leading even to an overestimation of the true mass. During the merger events, see Fig. 8, the bias is almost always positive, i.e. the HE mass is underestimating the true cluster mass. However, even with the highest bias value during the merger events, we can only come close to the bias suggested by Planck. Therefore, we need to look for other reasons for explaining this bias tension. The next-generation satellites, like XRISM (X-Ray Imaging and Spectroscopy Mission), hopefully Athena and the proposed probe LEM (Line Emission Mapper), but also eROSITA-data anal-

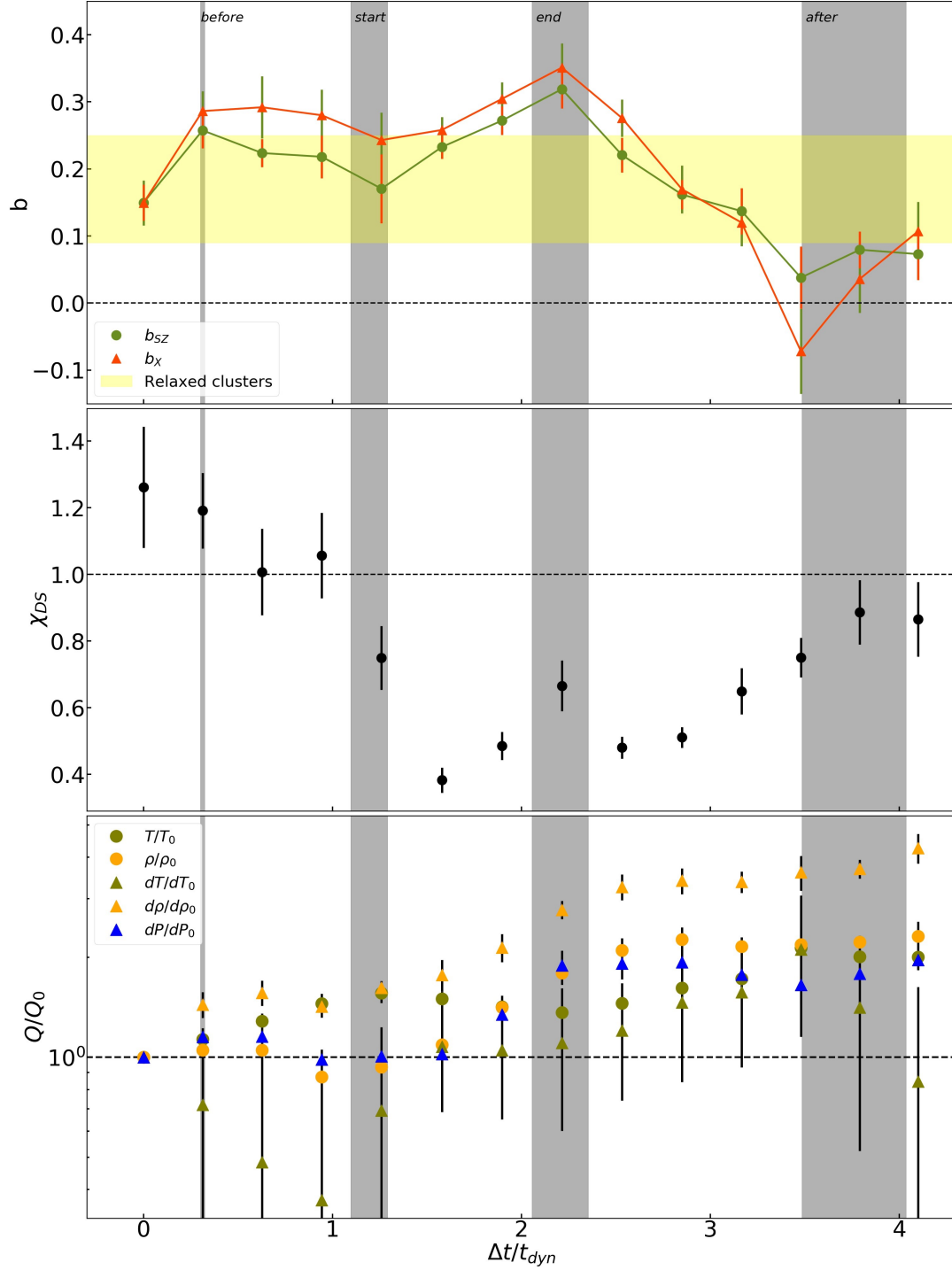


Figure 8. Top panel: the stacked biases at R_{200} (means and standard deviations) are represented as a function of the difference in times from t_0 , divided by the dynamical time. The SZ bias is represented in green, while the X one in orange. The yellow shaded region represents the biases range of the relaxed clusters. The null bias is represented with a dashed line. Central panel: the stacked relaxation parameter estimated inside R_{200} , the means and the standard deviations are represented as a function of $\Delta t/t_{dyn}$. The dashed line represents the threshold between relaxed and disturbed clusters. Bottom panel: each thermodynamic quantity which takes part in the estimation of the HE mass (and bias) divided by their value before the merger (indicated with a subscript 0) is shown as a function of $\Delta t/t_{dyn}$. The dashed line shows the value of 1 (the quantity does not change with respect to the age prior to the merger). The temperature and its derivative are represented in olive green dots and triangles respectively. Instead, the density and its derivative are represented as orange dots and triangles, and the pressure derivative is represented with blue triangles. In the plot the means and the standard deviations are represented. In all the panels, the vertical grey shaded areas represent the $\pm 1\sigma$ regions of the averaged time *before*, *after*, *start* and *end* of the merger.

ysis, are going to give precise indication on the gas velocities and dispersion and, consequently on cluster dynamical state.

ACKNOWLEDGEMENTS

The authors would like to thank the Referee for the constructive and helpful comments. The simulations used in this work have been performed in the MareNostrum Supercomputer at the Barcelona Supercomputing Center, thanks to CPU time granted by the Red Española de Supercomputación. WC is supported by the STFC AGP Grant ST/V000594/1 and the Atracción de Talento Contract no. 2020-T1/TIC-19882 granted by the Comunidad de Madrid in Spain. He further acknowledges the science research grants from the China Manned Space Project with NO. CMS-CSST-2021-A01 and CMS-CSST-2021-B01. GY acknowledges financial support from the MICIU/FEDER (Spain) under project grant PGC2018-094975-C21. MDP acknowledges support from Sapienza Università di Roma thanks to Progetti di Ricerca Medi 2019, RM11916B7540DD8D. AK is supported by the Ministerio de Ciencia, Innovación y Universidades (MICIU/FEDER) under research grant PGC2018-094975-C21 and further thanks Piero Umiliani for ‘svezia, inferno e paradiso’.

DATA AVAILABILITY

The data underlying this article were produced as part of THE THREE HUNDRED Project (Cui et al. 2018). They will be shared on request to THE THREE HUNDRED Collaboration, at <https://www.the300-project.org>.

REFERENCES

- Angelinelli M., Vazza F., Giocoli C., Etti S., Jones T. W., Brunetti G., Brüggemann M., Eckert D., 2020, *MNRAS*, 495, 864–885
- Ansarifard S., et al., 2020, *A&A*, 634, A113
- Arnaud M., Pratt G. W., Piffaretti R., Böhringer H., Croston J. H., Pointecouteau E., 2010, *A&A*, 517, 1
- Artis E., Melin J.-B., Bartlett J., Murray C., 2022, *EPJ Web of Conferences*, 257, 00004
- Barnes D. J., Vogelsberger M., Pearce F. A., Pop A.-R., Kannan R., Cao K., Kay S. T., Hernquist L., 2021, *MNRAS*, 506
- Bennett J. S., Sijacki D., 2022, *MNRAS*, 514, 313
- Biffi V., Sembolini F., De Petris M., Valdarnini R., Yepes G., Gottlöber S., 2014, *MNRAS*, 439, 588
- Bulbul E., et al., 2019, *ApJ*, 871, 50
- Campitiello M. G., et al., 2022, *A&A*, 665, A117
- Cialone G., De Petris M., Sembolini F., Yepes G., Baldi A. S., Rasia E., 2018, *MNRAS*, 477, 139
- Contreras-Santos A., et al., 2022, *MNRAS*, 511, 2897
- Cui W., et al., 2016, *MNRAS*, 456, 2566
- Cui W., Power C., Borgani S., Knebe A., Lewis G. F., Murante G., Poole G. B., 2017, *MNRAS*, 464, 2502
- Cui W., et al., 2018, *MNRAS*, 480, 2898
- Cui W., et al., 2022, *MNRAS*, 514, 977
- Davé R., Anglés-Alcázar D., Narayanan D., Li Q., Rafieferantsoa M. H., Appleby S., 2019, *MNRAS*, 486, 2827
- De Andres D., et al., 2022, *EPJ Web of Conferences*, 257, 00013
- De Luca F., De Petris M., Yepes G., Cui W., Knebe A., Rasia E., 2021, *MNRAS*, 504, 5383
- Etti S., Donnarumma A., Pointecouteau E., Reiprich H. T., Giodini S., Lovisari L., Schmidt R. W., 2013, *Space Sci Rev*, 177, 119–154
- Gianfagna G., et al., 2021, *MNRAS*, 502, 5115
- Haggar R., Gray M. E., Pearce F. R., Knebe A., Cui W., Mostoghiu R., Yepes G., 2020, *MNRAS*, 492, 6074
- Henson M. A., Barnes D. J., Kay S. T., McCarthy I. G., Schaye J., 2017, *MNRAS*, 465, 3361
- Hernández-Lang D., et al., 2022, *MNRAS*, 517, 4355
- Hoekstra H., Herbonnet R., Muzzin A., Babul A., Mahdavi A., Viola M., Cacciato M., 2015, *MNRAS*, 449, 685
- Klypin A., Yepes G., Gottlöber S., Prada F., Heß S., 2016, *MNRAS*, 457, 4340
- Koukoulippas N., Alonso D., Bilicki M., Peacock J. A., 2020, *MNRAS*, 491, 5464
- Kravtsov A. V., Borgani S., 2012, *ARA&A*, 50, 353
- Le Brun A. M. C., McCarthy I. G., Schaye J., Ponman T. J., 2017, *MNRAS*, 466, 4442
- Li Q., Han J., Wang W., Cui W., Li Z., Yang X., 2021, *MNRAS*, 505, 3907
- Mazzotta P., Rasia E., Moscardini L., Tormen G., 2004, *MNRAS*, 354, 10
- Nagai D., Kravtsov A. V., Vikhlinin A., 2007, *ApJ*, 668, 1
- Nagarajan A., et al., 2018, *MNRAS*, 488, 1728
- Navarro J. F., Frenk C. S., White S. D. M., 1997, *ApJ*, 490, 493
- Nelson K., Rudd D. H., Shaw L., Nagai D., 2012, *ApJ*, 751, 121
- Nelson K., Lau E. T., Nagai D., Rudd D. H., Yu L., 2014, *ApJ*, 782, 107
- Neto A. F., et al., 2007, *MNRAS*, 381, 1450
- Ntampaka M., Trac H., Sutherland D. J., Battaglia N., Póczos B., Schneider J., 2015, *ApJ*, 803, 50
- Okabe N., Smith G. P., 2016, *MNRAS*, 461, 3794
- Pearce F. A., Kay S. T., Barnes D. J., Bower R. G., Schaller M., 2019, *MNRAS*, 491, 1622
- Piffaretti R., Valdarnini R., 2008, *A&A*, 491, 71
- Planck Collaboration et al., 2016, *A&A*, 594, A13
- Pratt G. W., Arnaud M., Biviano A., Eckert D., Etti S., Nagai D., Okabe N., Reiprich T. H., 2019, *Space Sci Rev*, 215
- Rasia E., et al., 2012, *New Journal of Physics*, 14, 055018
- Rasia E., Borgani S., Etti S., Mazzotta P., Meneghetti M., 2013, *ApJ*, 776, 39
- Rasia E., et al., 2015, *ApJ*, 813, L17
- Salvati L., Douspis M., Aghanim N., 2018, *A&A*, 614, A13
- Salvati L., Douspis M., Ritz A., Aghanim N., Babul A., 2019, *A&A*, 626, A27
- Sembolini F., Yepes G., De Petris M., Gottlöber S., Lamagna L., Comis B., 2013, *MNRAS*, 429, 323
- Sereno M., Lovisari L., Cui W., Schellenberger G., 2021, *MNRAS*, 507, 5214–5223
- Tian Y., Cheng H., McGaugh S. S., Ko C.-M., Hsu Y.-H., 2021, *ApJ Letters*, 917, L24
- Vega-Ferrero J., Yepes G., Gottlöber S., 2017, *MNRAS*, 467, 3226
- Velliscig M., et al., 2015, *MNRAS*, 453, 721
- Vikhlinin A., Kravtsov A., Forman W., Jones C., Markevitch M., Murray S. S., Speybroeck L. V., 2006, *ApJ*, 640, 691
- Von der Linden A., et al., 2014, *MNRAS*, 443, 1973–1978
- Wicker R., Douspis M., Salvati L., Aghanim N., 2022, *EPJ Web of Conferences*, 257, 00046
- Zwicky F., 1937, *ApJ*, 86, 217

This paper has been typeset from a \LaTeX file prepared by the author.